Acta Materialia 269 (2024) 119804

Contents lists available at ScienceDirect

Acta Materialia

journal homepage: www.elsevier.com/locate/actamat

Mechanisms of structural evolution of laminates with immiscible components under high-pressure torsion

A. Mazilkin [a,b,*], V. Tavakkoli [a,c], O. Davydenko [d], Y. Beygelzimer [a,d], E. Boltynjuk [a], T. Boll [a,b,e], B. Straumal [a], B. Baretzky [a], Y. Estrin [f,g], R. Kulagin [a]

[a] Institute of Nanotechnology, Karlsruhe Institute of Technology, 76344 Eggenstein-Leopoldshafen, Germany
[b] Karlsruhe Nano Micro Facility (KNMFi), Karlsruhe Institute of Technology, 76344 Eggenstein-Leopoldshafen, Germany
[c] Department of Materials and Earth Sciences, Technical University of Darmstadt (TUD), 64287, Darmstadt, Germany
[d] Donetsk Institute for Physics and Engineering named after O.O. Galkin, National Academy of Sciences of Ukraine, 03028 Kyiv, Ukraine
[e] Institute of Applied Materials (IAM-WK), Karlsruhe Institute of Technology, Hermann-von-Helmholtz-Platz 1, 76344 Eggenstein-Leopoldshafen, Germany
[f] Department of Materials Science and Engineering, Monash University, Clayton, Victoria 3800, Australia
[g] Department of Mechanical Engineering, The University of Western Australia, Nedlands, WA 6009, Australia

ARTICLE INFO

Keywords:
Severe plastic deformation
High-pressure torsion
Turbulent flow
Mixing
Cu-Mo-Cu laminate
Self-similar structure
Finite element method

ABSTRACT

The mechanism of structural evolution of a three-layer Cu-Mo-Cu laminate under high-pressure torsion (HPT) was studied using scanning and transmission electron microscopy, atom probe tomography, and nanoindentation, complemented with finite element calculations. The results demonstrate a gradual refinement of the structure of the Mo component; a greater degree of refinement is observed in the peripheral part of the disk-shaped HPT specimen, although some heterogeneity of the structure remains even at a gigantic degree of shear deformation accumulated therein. The elemental distribution calculated from STEM-EDX mapping as well as 3D reconstruction of atom probe tomography results shows a significant degree of mixing of the sample components at the atomic level, the concentration of copper in molybdenum and molybdenum in copper reaching ~4.3 at.% and ~6 at.%., respectively. These observations correlate with nanoindentation results showing an increase in the hardness of both phases due to strain hardening and solid solution strengthening, as well as grain refinement. Numerical simulations made it possible to provide a detailed description of the stages of the structure fragmentation, including its self-organizing nature, to show the formation of rupture forerunners in the hard Mo layer, and the deformation of harder fragments in a softer matrix. The experimental results are supported by a model assuming a fractal self-organization of a self-similar structure during HPT processing.

1. Introduction

A key aspect of severe plastic deformation (SPD) is that it establishes geometrical conditions which prevent the sample from being damaged, enabling efficient deformation without any limitations on the attainable strain. This feature is common to all existing modes of SPD, including high pressure torsion (HPT) [1–6], equal channel angular pressing (ECAP) [3,7], equal channel angular pressing with the subsequent HPT (ECAP+HPT) [3], twist extrusion (TE) [8], planar twist extrusion (PTE) [9], planar twist channel angular extrusion (PTCAE) [10], equal channel angular pressing with subsequent cold rolling (ECAP + CR) [11], and constrained groove pressing (CGP) [12]. Although formally SPD-induced strain can increase indefinitely, concurrent relaxation processes lead to a kind of dynamic steady state. Indeed, it is well known that during SPD such characteristics as the grain size [13–21], the size of second-phase particles [22,23], hardness [10,14,21,24–37], and the lattice parameter of solid solutions [1,38–41] tend to saturation with increasing strain. It should be noted that different properties reach saturation at different strain values [22].

If the initial sample contains two or more phases, it is very intriguing how the fragmentation of these phases occurs during SPD processing. Before SPD, the initial material may (a) contain a mixture of powders of two phases, (b) consist of multiple alternating layers of two phases, or (c) include a second phase in the form of particles dispersed in the bulk or located along the grain boundaries as interlayers. In Refs [42–44] the first case was studied, namely HPT of a mixture of tungsten and copper

* Corresponding author.
E-mail address: andrey.mazilkin@partner.kit.edu (A. Mazilkin).

https://doi.org/10.1016/j.actamat.2024.119804
Received 3 December 2023; Received in revised form 13 February 2024; Accepted 27 February 2024
Available online 1 March 2024

powders with an initial particle size of 2–10 μm. During HPT, the initially equiaxed W particles first got elongated, and then broke up into smaller and less oblong ones. Finally, the grain size of tungsten decreased with an increase in the number N of anvil revolutions to a steady-state size of 10–20 nm at $N = 10$ [43]. In Refs. [45–47] the fragmentation of Cu and Co powders under HPT was studied. The initial size of the powders was 2–10 μm. It was reported that the microhardness saturated at $N \sim 4.5$, while the grain size of Cu and Co phases leveled off at about 200 nm after $N = 8$ [45,46]. Studies of the HPT of the liquid-metal infiltrated Cu-Mo, Cu-Cr and Cu-W composites showed that with the increasing number of the anvil revolutions, the original infiltrated mixtures first formed layered structures [23,48,49]. With further increase of shear strain, the layers broke and equiaxed Mo, Cr or W particles appeared. Eventually, a steady-state size of Cr and Mo particles was attained [23].

In Ref. [50] a Cu/Ti bimetallic nanocomposite was produced by the accumulative roll-bonding (ARB). Before ARB the initial thickness of copper sheets was 300 μm and that of titanium layers was 100 μm. The ARB process was repeated up to nine times with ~ 50 % thickness reduction after each pass. During ARB, the Ti layers ruptured and formed elongated particles. The elongation of the particles gradually decreased with increasing number of passes, N. The formation of shear bands intersecting the Ti layers was observed within the composite after $N = 3$. After $N = 7$ the size of Ti particles saturated at about 2 μm [22,50]. This value is much higher than the steady-state size of fragments in W-Cu and Co-Cu alloys after HPT described above [23,42–47]. This suggests that, in addition to the difference in the material pairs used, the mechanical conditions for the fragmentation during ARB and HPT are different.

A noteworthy example of the second-phase fragmentation during SPD can be found in studies of carbon steels [51–58]. Cementite platelets underwent transformations in several steps, first breaking, then spheroidizing, and in some cases being almost dissolved. These changes are closely related to the appearance of newly formed grain boundaries, which play a key role in the process of cementite transformation. The amount of cementite in steel is reduced because carbon forms segregation layers at the grain boundaries created during grain refinement as a result of SPD [59]. This “scavenging” of carbon from cementite particles ultimately leads to a decrease in the volume fraction of cementite.

In Ref. [60] the Al – 4 wt.% Fe alloy was treated by HPT up to $N = 75$. In the initial state, the samples contained Al_3Fe precipitates. Al_3Fe particles were continuously fragmented during HPT. Their size saturated at about 20 μm after $N = 10$ and remained unchanged for $N > 10$. Thus, the steady-state size of Al_3Fe particles during HPT [60] is one to two orders of magnitude greater than the particle size observed in Cu with W, Co, or Ti after HPT and ARB [44–46,50]. This strong difference in fragmentation behavior may be due to various factors, such as a difference in the volume fractions of the second phase and/or the difference in hardness of the second-phase particles and the matrix. In any case, phase fragmentation during SPD poses many open questions and requires a deeper study.

In recent studies, the possibility of mechanical alloying of immiscible components, such as, for example, Cu-W and Cu-Mo, under the influence of SPD was explored [43,61–64]. The data from different studies are often contradictory, which indicates the complexity of the processes occurring during SPD; the result of SPD processing may depend on many factors that are difficult to consider. It can be noted, for example, that ball milling of initial elemental components either does not lead to the formation of solid solutions [63], or the observed solubility is very low and hardly discernible given the measurement uncertainty [43,62,64]. It was also reported that this type of SPD leads to amorphization of the components rather than the formation of a solid solution [61]. In most studies, the occurrence of a solid solution is judged from the results of XRD analysis, such as a shift of the diffraction peak and the disappearance of the signal from the second component. It is therefore worth mentioning that in some studies the amount of the second component in the solution was determined – either by direct measurement or by using the empirically derived Vegard’s law. In particular, the authors of [64] applied HPT to a single phase Cu – 5 at.% Mo system under cryogenic conditions and observed the steady-state solubility of Mo in Cu at a level of less than 1 at.%.

Currently, there is no consensus among researchers regarding the mechanisms behind the structural evolution of laminates under HPT. One group of authors believes that the distortions observed in the layers during HPT (such as folds, vortices, ruptures, etc.) are purely mechanistic and are not related to the microstructure of the constituent materials [65]. They base their conclusion on numerical analysis using a model of nonlinear viscous fluids, which exhibits patterns similar to those occurring in geological structures at much larger spatiotemporal scales.

By contrast, molecular dynamics modeling suggests that the formation of waves and vortices during HPT of laminates is associated with the formation of disoriented "crystallites" whose size is commensurate with the layer thickness [66]. This implies that the microstructure might play a crucial role in pattern formation. Refs. [15,67] associate distortions in the regular geometry of laminates with localized hindrance to shear flow, leading to the loss of stability in laminar flow and the emergence of vortex movement. According to these ideas, the microstructure does influence the mechanism that inhibits shear flow, but its presence is not a prerequisite for the loss of stability in the harder layers.

The authors of [68] put forward a hypothesis that vortex formation can be explained by a defining property of solids – their ability to retain their shape and only change it when the applied stresses exceed a certain threshold level. This property fundamentally distinguishes solids from liquids and stems from the long-range order prevalent in the structure of solids. A discrete particle model for HPT of laminates was used in [68] to analyze the effect of the correlation radius of interparticle interaction on the character of the motion of the constituents of a laminate in response to shear under pressure. The ideas posited in [65–67] suggest that the patterns observed in laminates deformed by HPT at a macro scale can be attributed to the existence of a threshold value of the flow stress, such as the yield stress in plasticity theory or its analogue in the nonlinear viscous fluid model [69]. A distinctive view taken in [67,68] is that the physical reason for pattern formation is attributable to the presence of long-range order in the solid-state structure.

The approach employed in this study to investigate solid-state mechanical mixing involves a comprehensive analysis of both experimental data and computer modeling results within the framework of classical plasticity theory. For the experiment, a three-layer Cu-Mo-Cu laminate was taken, consisting of components that are practically immiscible up to temperatures exceeding 1000 °C. This allows us to neglect the influence of diffusion at the initial stage of the process, even if the heat generated by mechanical work is considered. Moreover, in a laminate with a selected pair of components, a harder layer is sandwiched between layers with lower hardness – a configuration that, as shown by our analysis, promotes the effect of mechanical mixing. In the present article it is shown for the first time that some prominent features of HPT of laminates can be adequately described in terms of plasticity theory. In particular, we consider the occurrence of constrictions in harder layers, which lead to repeated division of the layers into fragments with progressively decreasing dimensions. The validity of the proposed model does not specify the chemical composition or the microstructure of the co-deforming materials, which makes it possible to highlight the common principles of the solid-phase mixing process applicable to a broader range of metal laminates. The general nature and the specific mechanisms of fragmentation, as well as the existence of the smallest possible fragment size, will be discussed.

2. Experimental

2.1. Material and HPT processing

Commercially pure molybdenum (99.8 %) and copper (99.9 %) were used for HPT experiments. Samples in the form of disks with a thickness of 0.5 mm and diameter of 13 mm were obtained by cutting a rod. Without any special treatment, a stack of Cu-Mo-Cu, with a total thickness of ~ 1.5 mm, was placed between the anvils of an HPT rig. Processing of such three-layer laminates was performed on a standard HPT equipment (W. Klement GmbH, Lang, Austria). Quasi-constrained anvils with a diameter of 13 mm and a total anvil groove of ~ 0.6 mm were used. A pressure of 5 GPa applied vertically was controlled automatically throughout the entire test. The rotation speed of the anvil was 1 rpm. Processing was carried out at room temperature. The temperature of the sample during HPT was monitored using a portable non-contact laser pyrometer by directing the pyrometer beam to the contact zone between the sample and the anvil. According to our measurements, the temperature remained within the range of 40 – 60 °C throughout the entire deformation process. This low level of heating suggests that solute diffusivity was virtually unaffected by heat released during the HPT process. The results shown below refer to the number of the anvil rotation $N = 32$.

2.2. Microstructure characterization

For structural characterization of the deformed sample, scanning electron microscopy (SEM) was used. SEM study was performed on a ZEISS Auriga 60 scanning electron microscope using the back-scattered electron (BSE) detector. Samples for SEM investigation were prepared by cutting a disk-shaped HPT specimen in halves followed by mechanical grinding and polishing of the half-disk cross section with a series of diamond suspensions followed by 0.05 mm colloidal silica.

The structure of components of a three-layer sample in the initial state, i.e., Cu and Mo foils, was studied by means of electron backscatter diffraction (EBSD). EBSD maps were collected using an EDAX Digiview camera installed on ZEISS Auriga 60 SEM. Sample for EBSD studies were prepared by electro-chemical polishing on QATM - QETCH 1000 device. For Cu foils, the standard Struers D2 electrolyte was used at 5 °C and 5 V. For Mo foils, the electrolyte was 15 vol.% solution of H_2SO_4 in ethanol; the samples were polished at 2 °C and 15 V. EBSD patterns were recorded using the EDAX Apex 2.0 software. The step size for scanning was 0.5 μm. The recorded datasets were indexed using the OIM 8.6 software (EDAX).

Transmission electron microscopy (TEM) investigation was performed on a probe aberration corrected transmission electron microscope Themis 300 (ThermoFischer Scientific) operated at 300 kV. Elemental analysis was performed by energy dispersive X-ray spectroscopy (EDX) using a Super-X detector. Samples for TEM investigations were prepared by standard lift-out technique on FEI Strata 400 dual beam facility. The lift-out procedure was performed on the polished HPT half-disk cross section, which gave more control over the location where the TEM lamella was to be cut out.

ACOM examination was performed at 300 kV on Themis 300 equipped with NanoMegas ASTAR system for acquisition of orientation maps. The microscope was operated in micro-probe TEM mode with spot size 9, gun lens 6, and a 50 μm condenser aperture, and a camera length of 195 mm was used to acquire the diffraction patterns. This setup gave a nominal beam diameter of about 1.5 nm. The maps were acquired with 7 nm step size. Additionally, the beam was precessed around the optic axis of the microscope at an angle of 0.6 °

The Atom Probe Tomography (APT) analysis was carried out with a LEAP 4000X HR instrument at 40 K, with a laser pulse energy of 30 pJ, and a pulse rate of 125 kHz. The APT reconstruction and data evaluation was performed with the APT Suite software 6 (CAMECA/AMETEK). To prepare APT samples, a triangular lamella was extracted from the Cu matrix near the Mo particles at the edge part of the HPT sample using FIB lift-out method. The lamella was then cut into 3 samples, which were attached to the posts on a silicon coupon. Each sample was shaped into a needle using a Ga ion beam at 30 kV; final polishing was performed at 2 kV.

2.3. Nanohardness measurements

Nanohardness measurements were performed on the polished half-disk cross section of the HPT sample using an iNano Nanoindenter (KLA) equipped with a Berkovich-shaped diamond tip. Prior to nano-indentation, the instrument was calibrated using a standard fused silica reference sample. Continuous stiffness measurements were performed at room temperature with a constant strain rate of 0.2 s^{-1}. At least 10 indents per area with a maximum load of 10 mN or a depth of 300 nm were performed. The distance between the indents was~ 25 μm, large enough for the measurements at neighboring points not to affect each other. The positions of the imprints were somewhat different from those assigned before the measurements, therefore SEM-BSE images in the areas of indentation were collected to correlate the position of the imprints with the phases within the sample. More information on nanohardness measurements can be found in the Supplementary Information.

2.4. Finite element method (FEM)

Numerical experiments were performed using the commercial QForm software package [70]. The computations were conducted for a two-dimensional HPT model, which, in the first approximation, corresponds to the deformation of the annular elements of the sample located far enough from the axis of rotation.

The deformation process of laminates during HPT can be divided into two stages. At the initial stage, the layers undergo plastic deformation, leading to their distortion and fragmentation of the hard component into separate pieces. These fragments become encased within softer material. The second stage involves the plastic deformation of these fragments causing them to break down further into smaller pieces, which are spread over the sample volume by material fluxes.

The computational model for the initial stage is represented schematically in Fig. 1a. It is a thin three-layer sample confined between two plates, the lower of which is stationary, and the upper moving tangentially to the right at a constant speed. A constant force pressing the upper plate to the sample is applied vertically. The following geometrical parameters of the layers were used in the simulation: length $l_0 = 10$ mm, thickness $h_0 = 0.2$ mm. Each layer was segmented into 5000 three-node triangular finite elements, with at least ten elements across the thickness. The mesh was automatically reconfigured when the elements became strongly distorted at large strains. The material of the upper and lower layers (copper) and that of the middle one (molybdenum) sandwiched between them was considered to be isotropic and elastoplastic, obeying the von Mises plastic flow condition. The deformation curves for Cu are available in the QForm database. The stress-strain curve for Mo was taken in the form of the Ludwik equation $\sigma = \alpha(e_0 + e_M)^n$, where σ is the flow stress and e_M is the von Mises equivalent strain; the values of the parameters entering this power-law dependence were set at $\alpha = 605$ MPa, $e_0 = 0.0012$, and $n = 0.18$ [71]. The confining plates were considered as being infinitely rigid. Siebel's friction law with a constant value of the friction coefficient equal to 1 between the plates and the sample, as well as between the layers of the sample, was assumed. The velocity of the tangential movement of the upper plate was taken equal to 0.7 mm/s, and the magnitude of the vertical force applied to it was set at 70 tons.

The geometric model used to study the deformation of a harder fragment in a softer matrix (second stage) is shown in Fig. 2a. For the FEM calculations it was postulated that the vertical force and the plate velocity retain the same values as at the initial stage. The matrix was segmented into 50,000 – 150,000 three-node triangular finite elements,

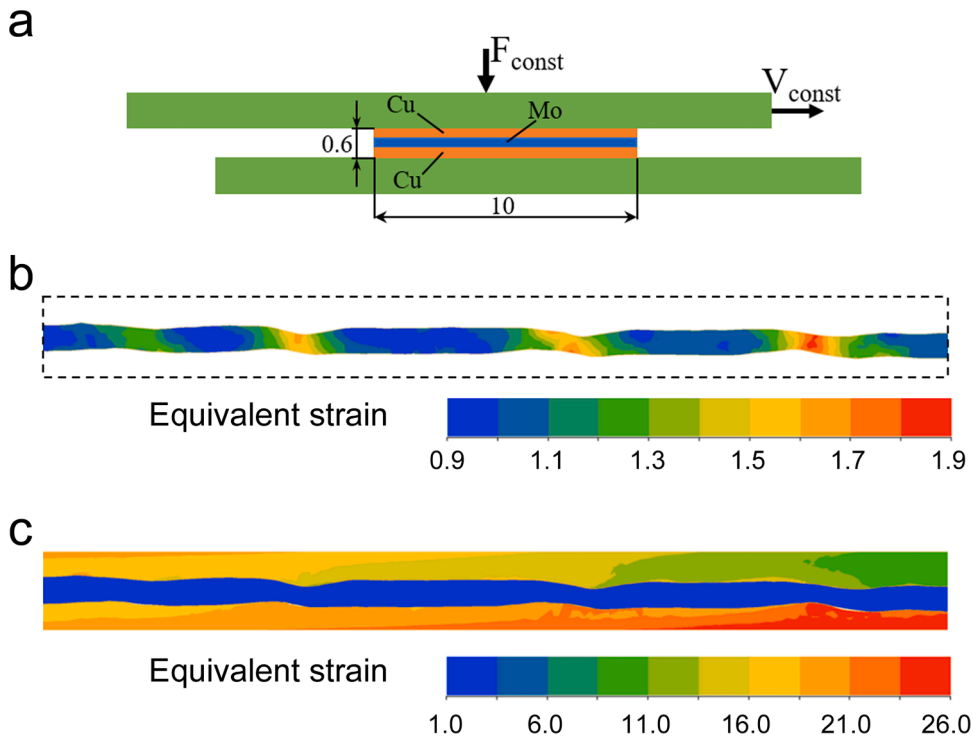

Fig. 1. Schematics for computational FEM experiment. (a) Two-dimensional three-layer model for HPT. Spatial distribution of the equivalent von Mises strain calculated by QForm FEM simulations for (b) Mo and (c) Cu and Mo layers.

while the fragment was segmented into 400 – 5500 elements depending on deformation conditions. The materials of the matrix and the harder inclusions were assumed to be rigid-plastic, excluding the quenching effect. Throughout numerical simulations, the geometric dimensions and the yield strength ratio of the two phases were set according to Fig. 2b-e.

3. Results

3.1. Microstructure of the material in the initial state

The microstructure of Mo and Cu in the initial non-deformed state was characterized using the orientation image mapping. The corresponding inverse pole figure (IPF) maps drawn based on the EBSD data are shown in Fig. S1. Molybdenum is characterized by ⟨110⟩ preferred orientation. The grain size population exhibits a quasi-binary distribution, with the average grain sizes of ~10 μm and ~28 μm for the small and the large grain fractions, respectively. The IPF map for Cu shows a structure typical for this material with the presence of numerous twins. A grain size distribution is close to the normal Gaussian shape with a mean grain size of ~ 32 μm. The microstructure of the laminate in the initial state serves as a reference for further comparison with the deformation-induced microstructure.

3.2. Structure of the deformed sample

3.2.1. SEM

Fig. 3 is an SEM overview image of the three-layer Cu-Mo-Cu sample after the HPT deformation (half sample shown). The image is a panoramic one constructed from several individual images, which were acquired using BSE detector sensitive to the material contrast, so the Mo phase is seen brightly against the Cu-phase background. It can be seen easily how the structure changes depending on the applied stress from the sample center (left) to its edge (right). Large fragments of the Mo phase are crushed into smaller pieces. The degree of comminution increases continually, so that in the edge regions of the sample an almost uniform distribution of Mo particles in the copper matrix is observed at this magnification scale.

To characterize the material in a more quantitative way, we studied the Mo particles distribution in Cu at three different locations in the HPT sample, *viz.* at the center of the sample, in the middle of its radius, and at its edge, so that the structure evolution depending on the amount of strain applied to the material could be followed. The results are presented in Fig. S2 and summarized in Table 1. We determined the volume fraction of the Mo phase. In addition, the size distributions for 'large' and 'small' Mo particle subsets were plotted separately. Indeed, the difference in size for these two subsets is huge, and it makes no sense to lump them together in a singular distribution. It should be noted, however, that subdivision into the two subsets was not free from some arbitrariness. Phase separation and quantification was carried out based on the contrast variation between the two phases using the plug-in of the ImageJ software package. According to the data obtained, the volume fraction of Mo phase varies from the center to the edge of the sample from 0.38 to 0.25, which is consistent with the ratio of the two constituents in the initial non-deformed sample (Cu/Mo = 2/1). The measured deviation from this ratio is caused by the large heterogeneity of the material distribution (especially in the middle of the sample); a further factor is the limitation of the method regarding detection of small molybdenum particles (notably at the sample edge). The particle size for both subsets of the Mo phase decreases from the center to the edge (see Table 1). We additionally calculated the fraction of the 'small' Mo particles among the whole Mo phase, considering this parameter as a characteristic of the material mixing. It varies from several percent at the center of the HPT disk to ~ 80 % at its edge. The variation of both quantities (the volume fraction of 'small' particles and the average particle size) with the distance from the rotation axis is tantamount to their variation with shear stress. The results thus demonstrate the effect of the shear deformation under HPT on material fragmentation and mixing.

3.2.2. ACOM TEM

To get more insight into the details of the sample structure, we

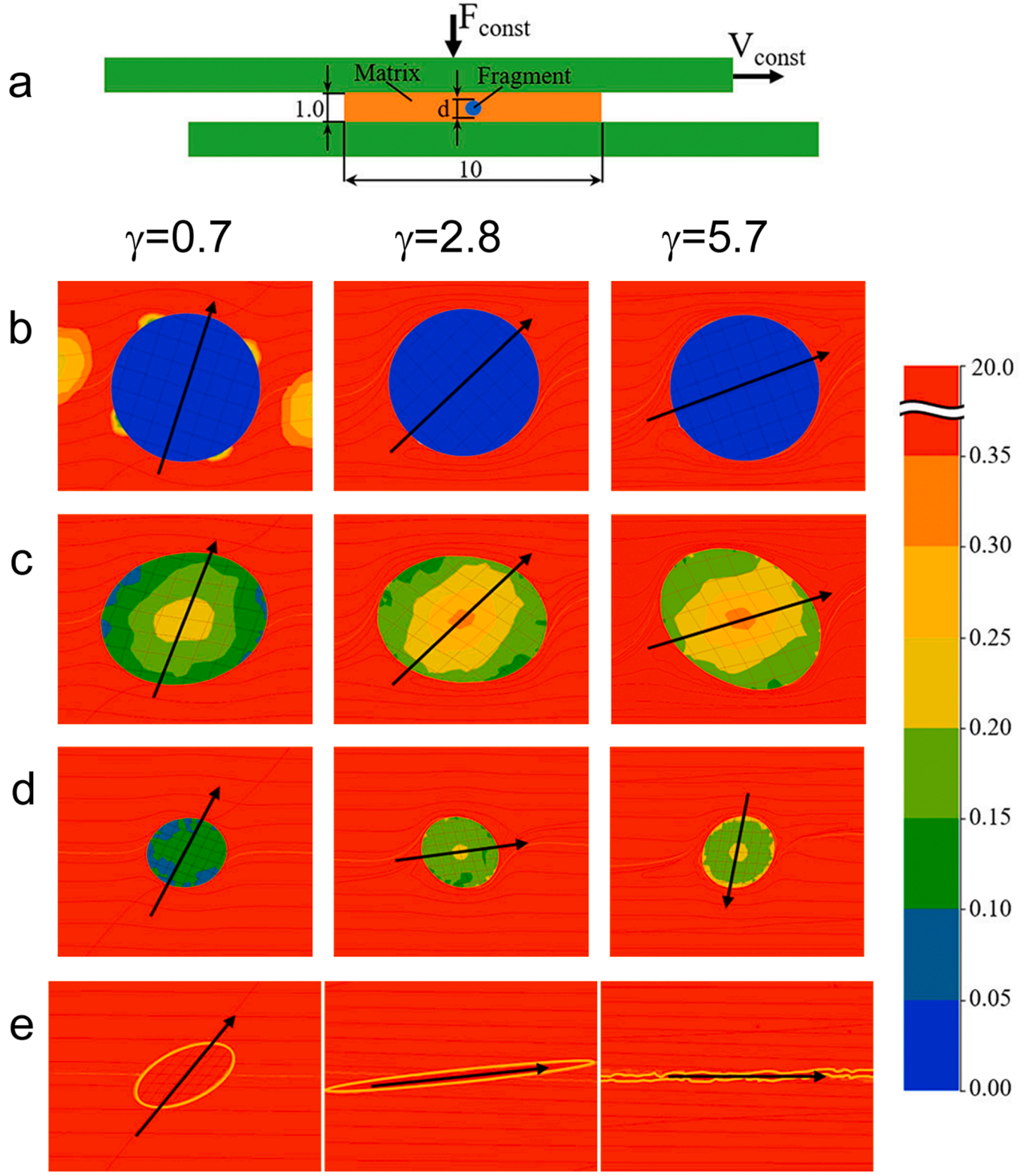

Fig. 2. (a) Schematics of an individual fragment of the hard phase in a soft matrix for a computational FEM experiment. Variants of the behavior of a hard fragment in a soft material for different shear ($\gamma = 0.7$, 2.8, and 5.7) and combinations of the parameters ξ and ς: (b) $\xi = 0.4$, $\varsigma = 0.3$; (c) $\xi = 0.4$, $\varsigma = 0.7$; (d) $\xi = 0.2$, $\varsigma = 0.7$; and (e) $\xi = 0.2$, $\varsigma = 1$. Here, as in the text, ξ and ς denote the dimensionless quantities associated with the fragment size and the hardness of the environment, respectively. The color code bar shows the magnitude of the von Mises equivalent strain. It should be noted that here the shear strain γ represents the additional strain increment applied to the sample after it was sufficiently pre-deformed to get fragmented and form a piece of hard phase in the soft matrix.

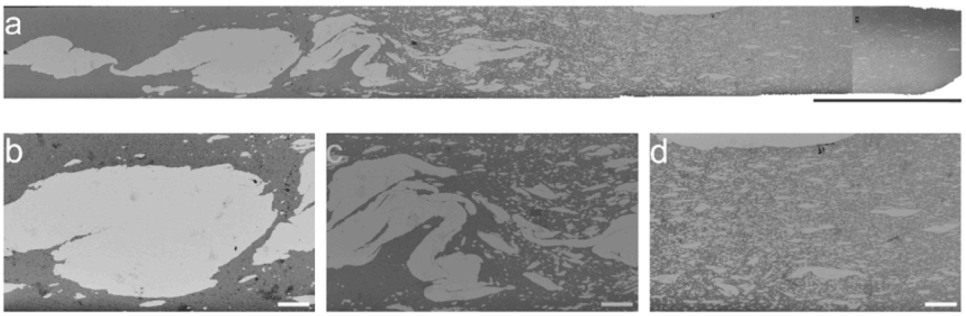

Fig. 3. (a) An overview SEM-BSE image of a Cu-Mo-Cu sample after the HPT deformation; the scale bar corresponds to 1 mm length. (b – d) SEM-BSE images of Cu-Mo-Cu HPT sample at higher magnification for (from left to right) central, mid-radius, and edge parts of the sample; the scale bar corresponds to 100 μm length.

Table 1
Results of the SEM image quantification (see Fig. 3); average size of big and small Mo particles (μm), fraction of Mo phase, and fraction of small Mo particles.

	Average particle size		Mo phase fraction	
	Small particles	Big particles	Total fraction	Small particles
Center	11	383	0.38	0.04
Mid-radius	2.3	18	0.38	0.42
Edge	1.3	11	0.25	0.79

performed an in-depth TEM study. Since the structure seen in the SEM-BSE images did not reveal any significant variation in the area near the edge of the sample, an observation of the structure at a distance of ¾ of the radius from its center was carried out in addition to that at the three above-mentioned points (center, mid-radius, and edge).

First, we applied the ACOM TEM method to reveal the material fragmentation caused by the HPT deformation. The result of the ACOM TEM mapping is shown in Fig. 4. The left column of the Figure depicts the phase – image quality (IQ) maps for various locations within the sample. The pixels with low IQ show the positions of grain boundaries (see black lines in the maps). It is seen from the maps that both constituent phases are gradually refined in the direction from the center to the edge of the sample. Furthermore, on the maps in Fig. 4c and d small molybdenum particles separated from the large phase pieces and distributed within the copper matrix are discernible. The grains of Mo after the deformation appeared strongly elongated, while those of Cu were closer to the equiaxed shape. The data on the grain size distribution (Fig. S3) provides qualitative characteristics of the material after various amounts of strain. As seen from the size distribution plots and the data in Table 2, the size of Cu grains gradually decreases from the center to ¾ of the radius, leveling off at this point at an average value of ~ 166 nm. For the Mo phase, we again calculated separately the grain sizes of large grains in big Mo chunks and of small particles dispersed in the Cu matrix (the latter for ¾-radius and edge only). It follows from the data in Table 2 that a gradual decrease of Mo grain size with the distance from the center occurs for the grains in large fragments, while a steady-state value for small Mo particles is established. The shape of the distributions is also different for the two material constituents. It is either bimodal (Fig S3b) or log-normal (Figs S3c and S3d for big Mo grains), while a Gaussian distribution is found for Cu and the small Mo grains.

3.2.3. TEM & HRTEM

Finer features of the sample microstructure were revealed by means of TEM, see Fig. 4. From the images acquired at lower magnification (middle column), we can judge the degree of phase mixing in the sample. One can see an approx. 30 nm wide gap between the two constituent layers of the sample at its center and at mid-radius, while the phase boundary looks uniform at the two other test points. HRTEM micrographs (Fig. 4, last column) show that the gap is not very densely filled with irregularly shaped particles. Based on analysis of the Fast Fourier Transform (FFT) from the phase boundary area, the particles were identified as Cu_2O oxides with cubic structure. They are usually formed on the surface of copper; the particles of this phase penetrate deeper into the sample as a result of mixing during deformation. For the samples prepared from the regions at ¾-radius and at the edge, the phase contact looks very smooth in the HRTEM micrographs. A closer inspection of the area near the boundaries between Mo and a Cu grains revealed that the contact between the two materials is established on the atomic scale.

3.2.4. STEM-EDX

The process of the mechanically induced element mixing was also studied by means of STEM-EDX mapping. The maps collected from the different regions of the HPT specimen are displayed in Fig. 5 together with the elemental profiles. In the sample taken from the central part a certain level of Cu solubility (~ 1.7 at.%) in Mo phase is attained, while the amount of Mo dissolved in Cu is negligible (see the corresponding profile and Table 3). Similar behavior is observed for the sample taken from the mid-radius where a noticeable grain refinement occurred; the Mo-based solid solution contains ~ 3 at.% of Cu. By contrast, at the edge of the HPT specimen, a distinctly higher content of both components in the counterpart-based solid solutions is found. The profile shows rather large variation of the solutes, which is most likely due to the inclination of the interphase boundary to the surface and the effect of the composition averaging through the sample thickness. We determined the composition based on several points in single-phase areas of the map. The average amount of Mo dissolved in Cu is ~ 6 at.%. The concentration of Cu in Mo-based solid solution reaches a value around 4.3 at.%. These levels of mutual solubility are extraordinarily high compared to the equilibrium binary phase diagram. Indeed, according to the reference data [72], the system is characterized by a very limited terminal solid solution: Cu at 1083.4 °C contains 0.067 at.% Mo, while Mo at 2515 °C contains 2.6 at.% Cu. By comparing these data with the observations of microstructure changes in the sample, we can conclude that real material mixing at the atomic scale takes place when a certain strain level is reached, and the two constituents of the layered material come into close contact with each other.

Another interesting feature in the map in Fig. 4c is the gap containing the Cu phase inside a Mo island. This feature can potentially offer insights into the process of material mixing that occurs during HPT deformation. In a copper - molybdenum pair, Mo is the more brittle material. The strain that accumulates over time can lead to the formation of cracks, which propagate within the Mo phase upon further deformation. This causes a gap to form within Mo which then gets filled with more ductile copper. Gradually, part of the molybdenum phase may become separated from a big piece, got fragmented and then dispersed throughout the copper matrix.

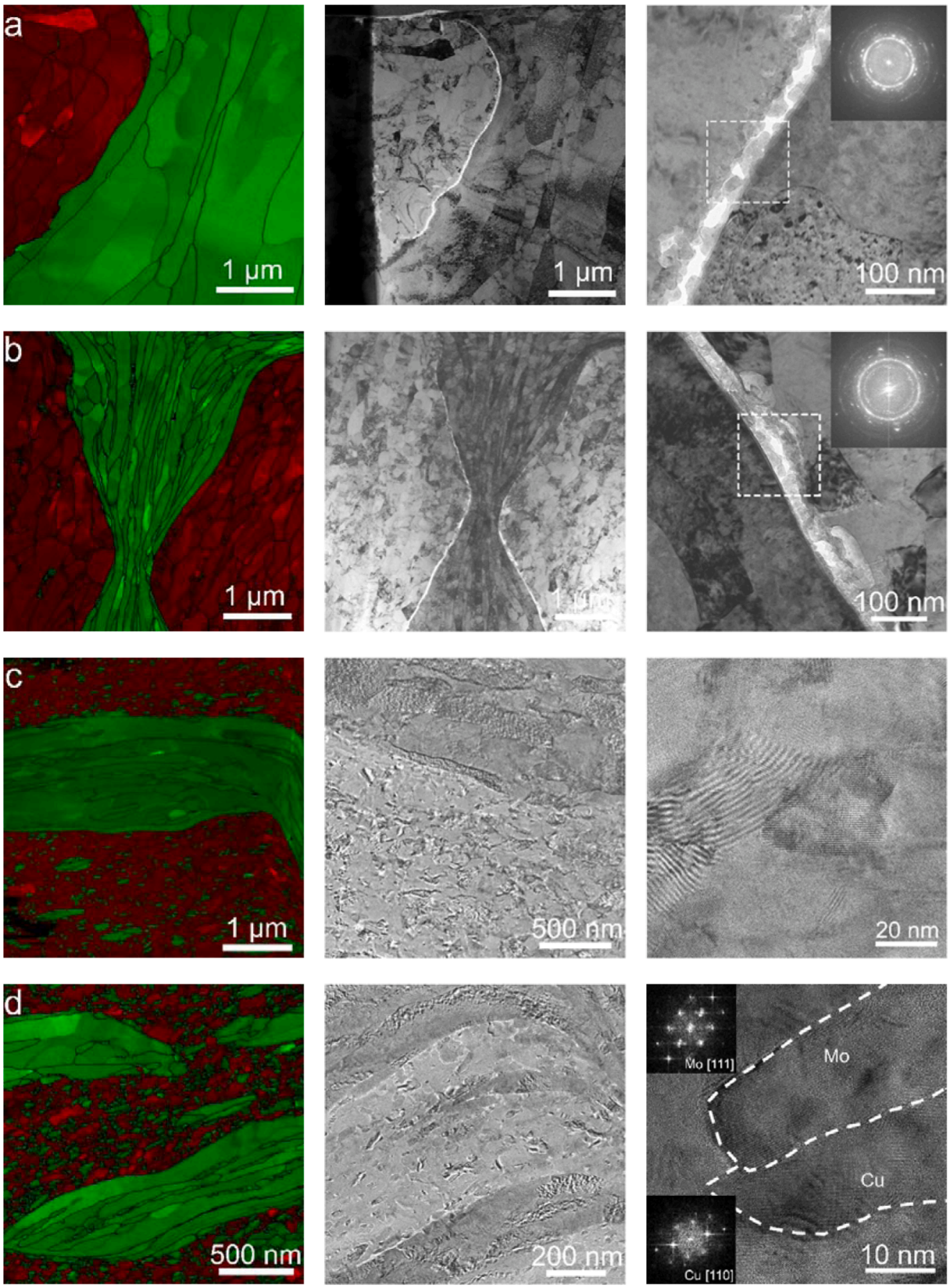

Fig. 4. (left column) combined ACOM TEM phase – IQ maps for (a) center, (b) mid-radius, (c) ¾ of radius and (d) edge of the Cu-Mo-Cu sample after HPT deformation. The Mo phase is highlighted in green and that of Cu in red. (middle column) TEM low magnification overview micrographs and (right column) HRTEM images of the samples from different locations of the Cu-Mo-Cu disk after HPT deformation. The insets in (a) and (b) are the Fast Fourier Transforms from the area near the Cu/Mo boundary (white dashed squares) and (d) from individual grains marked by dashed lines. The phase recognition was done based on the FFT pattern analysis.

Table 2
Results of the ACOM TEM data evaluation (see Fig. S2); average size of Cu and Mo grains (nm); the data for Mo in big and small particles are presented separately.

	Average Cu grain size	Average Mo grain size	
		Big particles	Small particles
Center	410	1200	
Mid-radius	310	390	
¾ of radius	166	226	53
Edge	164	126	48

3.3. Atom probe tomography

We also used APT to measure the solute concentration in both Cu and Mo phases more accurately and to eliminate the potential influence of test geometry (when the interface is inclined to the beam) and overlapping (when small particles of one phase contribute to the apparent solute content of the other phase). Fig. 6 shows the distribution of Cu and Mo for the reconstructed volume of a sample. The map in Fig. 6a demonstrates virtually no distinctive features since the APT tip was extracted from the Cu matrix, which is the main component of the sample. Several Mo particles of irregular shape highlighted by 9 at.% iso composition surfaces are seen in the bulk of a Cu-based solid solution (Fig. 6b). The composition of the Mo phase was determined based on the analysis of each individual particle, see the proxigram in Fig. 6c. The average solid solution concentration was determined to be ~5 at.% Cu in Mo and ~2 at.% Mo in Cu. However, the latter concentration reached ~5 at.% near the Cu/Mo interface. We can thus conclude that both the APT and the EDX measurements returned similar values for the concentration of solutes in the layered material considered. Finally, it should be noted that both EDX and especially APT are rather local methods for measuring solute concentrations. Therefore, we also carried out complementary X-ray diffraction measurements on a set of Cu-Mo-Cu laminates after HPT deformation with different numbers of anvil rotations. The dependence of solute solubility on shear strain measured by XRD is the subject of our forthcoming publication.

3.4. Results on nanoindentation

To measure the hardness of the Mo phase, indents were made inside large particles for all three locations on an HPT disk. When doing the measurements in Cu, it was difficult to make the indents isolated inside this phase, especially in the edge part of the sample; some of them were located near the Cu/Mo interface or even extended into Mo particles. Additionally, it is important to note that fine Mo particles with an average size of ~ 50 nm distributed in Cu matrix cannot be discerned in SEM-BSE images, although they certainly contribute to nanohardness.

The results of the measurements can be found in Table 4. Here we show the average value of nanohardness for Mo and Cu at the center, mid-radius, and edge regions of an HPT disk. From these data it can be clearly seen that both phases are hardened during HPT and the hardness is steadily increased with the increase of the strain. The mechanism involved in the hardening of both phases can be associated with (i) strain hardening, (ii) grain refinement (the Hall-Petch effect), and (iii) solid-solution hardening. For the Cu phase near the edge of the HPT sample, uniformly distributed fine Mo particles also act as obstacles to dislocation glide and, accordingly, raise the hardness. Comparison with the reference published data demonstrates that the hardness of the

Table 3
Content of solute elements in solid solutions in the HPT deformed sample (in at. %) as derived from the EDX mapping.

	Cu-based solid solution	Mo-based solid solution
Center	0.9	1.7
Mid-radius	0.3	3.0
Edge	6	4.3

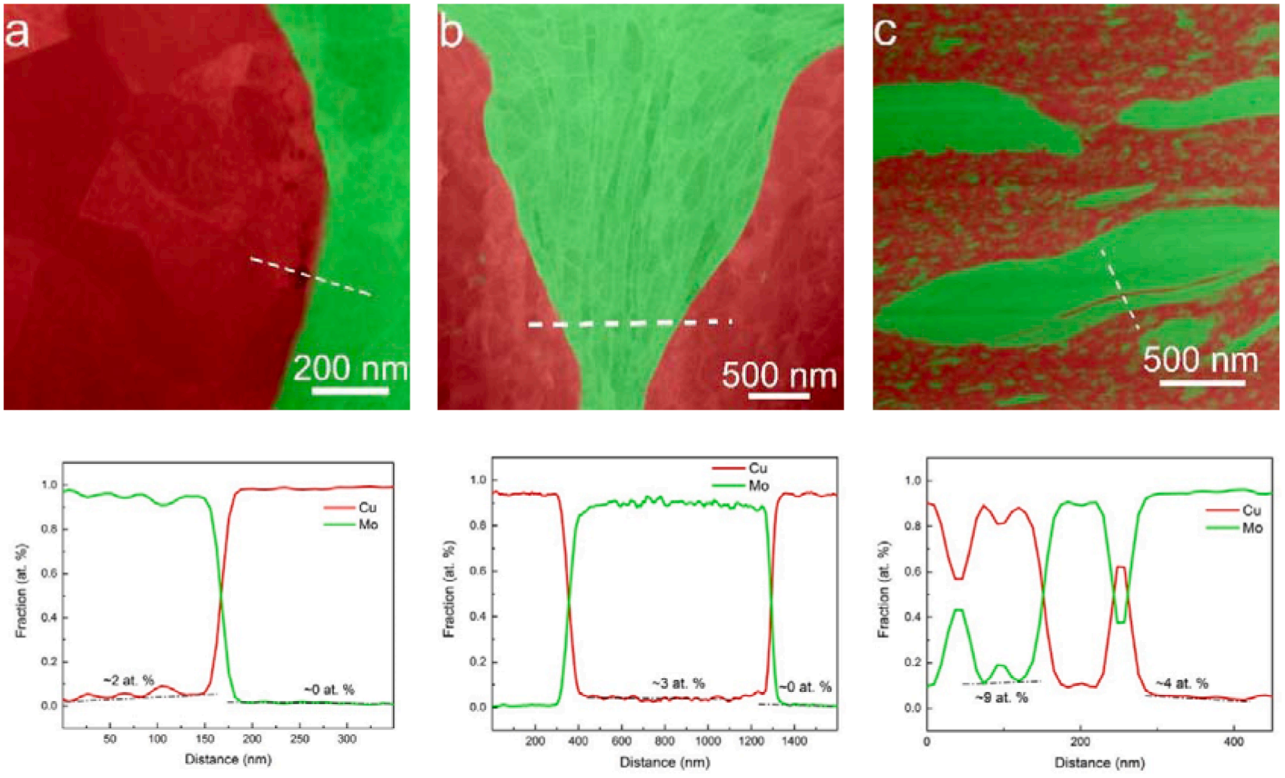

Fig. 5. STEM-EDX elemental maps from (a) center, (b) mid-radius, and (c) edge of the Cu-Mo-Cu disk after HPT deformation with the corresponding elemental profiles acquired along the lines shown in the maps.

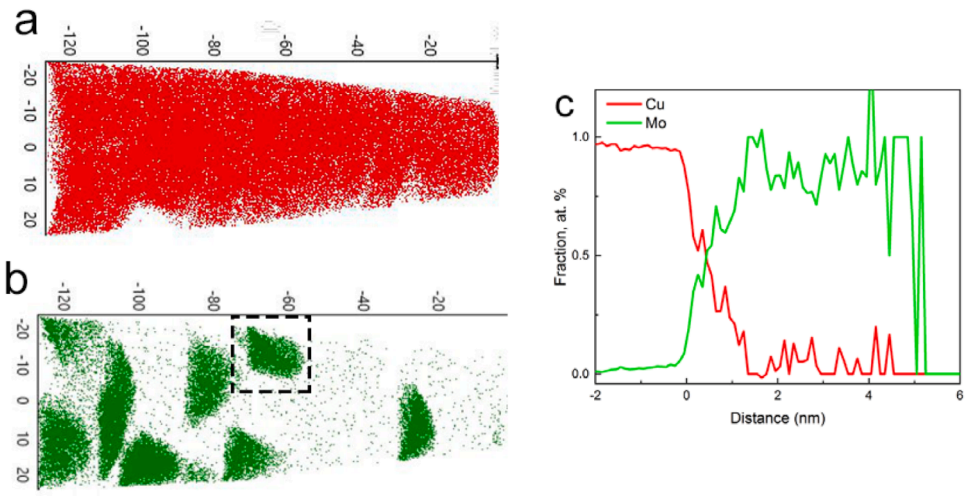

Fig. 6. 3D reconstructed volume of an APT specimen prepared from the edge of the Cu-Mo-Cu disk after HPT deformation showing the distribution of (a) Mo and (b) Cu; the units along the axes are nanometers. (c) a proxigram of the particle marked with the dashed black rectangle in (b) representing the concentration profile vs. the distance from the interface marked by the 9 at.% Mo isosurface.

Table 4
Hardness (GPa) of Cu-Mo-Cu sample at different locations and for different phases and the data for pure Cu and Mo after HPT for comparison. Values in HV were converted to GPa by multiplying by a factor of 9.8 [83] except for data in Ref. [84].

	Center	Mid-radius	Edge	Pure non-deformed components	Pure components after HPT
Mo	8.0 ± 0.3	8.5 ± 0.7	8.7 ± 0.6	3.0 [84]	6.6 [85] 5.1 [86] 7.8 [84]
Cu	2.5 ± 0.7	2.9 ± 0.7	4.1 ± 0.6	0.51 [87]	1.6 [88] 1.2 [2] 1.4 [89] 1.4 [90]

phases in the HPT-processed laminate sample is noticeably higher for Mo, and it is almost three times higher for Cu. However, an interesting observation in the indentation maps should be mentioned: for several imprints inside the Mo phase the hardness values were significantly lower than the average value, cf. Fig. S4. This is consistent with the finding that, unlike sub-micron sized dispersed particles, large ones do not contribute to particle strengthening, see e.g., Ref. [73].

3.5. FEM computations results

3.5.1. Initial stage of deformation: distortion of layers and formation of forerunners for hard layer ruptures

The computation results are presented in Fig. 1 which displays the distribution of the von Mises equivalent strain in Mo (Fig. 1b) and in all three layers (Fig. 1c) after shear strain $\gamma = s/H_0 = 14.2$, where s is the horizontal displacement of the top plate and H_0 is the initial sample thickness.

The forerunners of ruptures of the hard molybdenum layer are clearly visible in Fig. 1 in the form of localized deformation sites whose spacing is a multiple of the layer thickness. This result agrees with experiment [67] and, together with the general analysis presented above, it is a convincing argument in favor of the macroscopic character of the fragmentation of the harder layer.

3.5.2. Second stage: deformation of a harder fragment in a softer matrix

Tracking objects (arrays of lines) were applied to the model used for computer simulation to monitor the change in the shape of the fragment during deformation. To visualize the variation of the orientation of the fragment in the plane of the model, we used an arrow, which in the initial state was directed vertically upwards.

The following notation was used to characterize the fragment and the matrix: σ_f and σ_m denote the flow stresses of the fragment and its environment, respectively, H is the distance between the plates (the sample thickness), and d is the characteristic size of the fragment. For the description of the fragment and the environment, two non-dimensional parameters, $\xi = d/H$ and $\varsigma = \sigma_m/\sigma_f$ were introduced. The results of the computational experiments for several values of these parameters are shown in Fig. 2. For example, a large inclusion ($\xi = 0.4$) in a soft matrix ($\varsigma = 0.3$) does not deform, but only rotates as a whole in the shear flow (see Fig. 2b). In a harder matrix ($\varsigma = 0.7$), the same inclusion not only rotates, but also deforms (Fig. 2c). When the inclusion diameter is smaller ($\xi = 0.2$), it experiences more rotation than distortion (cf. Fig. 2c and Fig. 2d). A particle with the same flow stress as the matrix ($\varsigma = 1$) is deformed almost in the same way as the surrounding matrix itself (Fig. 2e). The results of the calculations showing the structural changes in Cu-Mo-Cu laminates as well as those of the FEM are discussed and analyzed below.

4. Discussion

It is important to summarize some general patterns of evolution of the laminate structure considered during HPT and the underlying mechanisms. To that end, we analyze the results of real and computational experiments described in the foregoing section.

We start with a qualitative analysis of the characteristic features of the stress-strain state (SSS) of hard and soft layers. This should help in understanding the mechanisms leading to their distortion and, ultimately, to fracture. We use the approximate estimates of the stresses and

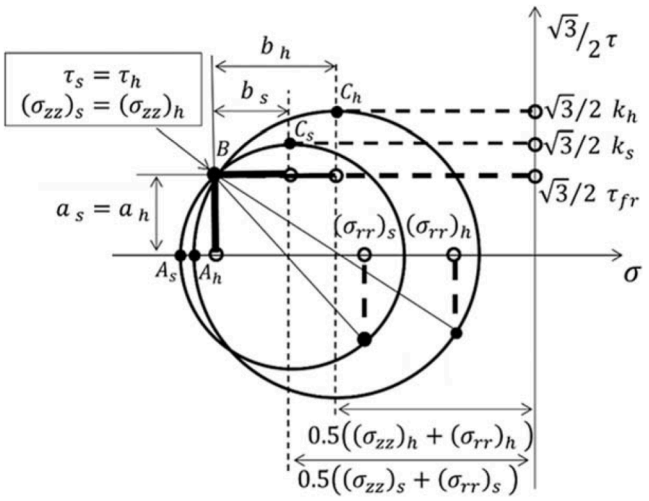

Fig. 7. Graphical representation of the SSS of laminates under HPT. The notation is explained in the text.

strain rates during HPT obtained in Ref. [74], and the procedure proposed therein for geometric mapping of the SSS characteristics of a sample. The respective geometric constructions for the hard and the soft layers are shown in Fig. 7.

According to [74], the two circles in Fig. 7 correspond to an approximate plasticity condition

$$f = (\sigma_{zz} - \sigma_{rr})^2 + 3\tau^2 - 3k^2 = 0 \tag{1}$$

for both the hard and the soft materials (corresponding to the larger and smaller circles, respectively). In this expression, the shear stress τ in a plane normal to the z axis is given by $\tau = \sqrt{\sigma_{zr}^2 + \sigma_{z\theta}^2}$. The quantities σ_{zz} , σ_{rr} , σ_{zr} , $\sigma_{z\theta}$ are the components of the stress tensor in cylindrical coordinates, with the z-axis coinciding with the sample axis. In Eq. (1), k denotes the flow stress of the material under shear deformation. The condition expressed by Eq. (1) was obtained under certain assumptions, one of which is the fulfillment of the equality $\sigma_{rr} = \sigma_{\theta\theta}$. The subscripts h and s in Fig. 7 refer to the hard and the soft material, respectively.

According to [75], under plastic co-deformation of hard and soft layers the normal and tangential stresses at the interface do not have a discontinuity, therefore the equalities $(\sigma_{zz})_s = (\sigma_{zz})_h = \sigma_{zz}$, $(\sigma_{zr})_s = (\sigma_{zr})_h$, $(\sigma_{z\theta})_s = (\sigma_{z\theta})_h$ are fulfilled. These conditions are satisfied at the interception point B of the two circles where $\tau_s = \tau_h = \tau_{fr}$ holds. Here τ_{fr} is the friction stress acting between the sample and the anvils. It is seen from Fig. 7 that the inequality $(\sigma_{rr})_h > (\sigma_{rr})_s$ holds, meaning that during co-deformation in the region of plasticity, the hard layer is stretched with respect to the soft ones. Here we are talking about *relative* tension, since the entire sample is under high hydrostatic pressure, so that both stresses are negative and noticeably large, see Fig. 7.

As shown in [74], the lengths of segments a and b are related to the shear rate $\dot{\gamma} = \sqrt{\dot{\gamma}_{zr}^2 + \dot{\gamma}_{z\theta}^2}$ and the axial deformation rate $\dot{e}_{zz}$ through the following equations:

$$a = |\dot{\gamma}| \Big/ 4\sqrt{3}\lambda \tag{2}$$

$$b = |\dot{e}_{zz}|/4\lambda, \tag{3}$$

where $\lambda > 0$ is a material parameter. According to Fig. 7, the following relations hold during the co-deformation of hard and soft layers: $a_h = a_s$, $b_h > b_s$. From Eqs. (2) and (3) it then follows: $|\dot{\gamma}_h| = |\dot{\gamma}_s|$, and $|(\dot{e}_{zz})_h| > |(\dot{e}_{zz})_s|$. With $\dot{e}_{zz} \le 0$, the following inequality is obtained:

$$(\dot{e}_{zz})_h < (\dot{e}_{zz})_s \tag{4}$$

The inequality (4), combined with the volume constancy condition ($\dot{e}_{zz} + \dot{e}_{rr} + \dot{e}_{\theta\theta} = 0$), and with the assumption that $\dot{e}_{rr} = \dot{e}_{\theta\theta}$ (see Ref. [74]), leads to the following relations: $(\dot{e}_{rr})_h > (\dot{e}_{rr})_s \ge 0$, $(\dot{e}_{\theta\theta})_h > (\dot{e}_{\theta\theta})_s \ge 0$. As was discussed above, they indicate that the hard layer experiences biaxial tension in its plane, being more stretched with respect to the soft layers. We believe that this leads to the occurrence of localized deformation zones in the hard layer causing ruptures therein; the penetrating material of the soft layers immediately fills the gaps thus formed. This scenario is consistent with the structure evolution observed in [67].

Furthermore, Fig. 7 enables one to obtain an interesting result regarding the direction of the maximum shear. At the top of the circle where $\tau = k$ (the points C_h and C_s for hard and soft material, respectively), the plane with the maximum shear stress and the maximum shear rate is parallel to the layers. At the leftmost point $\tau = 0$ (the points A_h and A_s for hard and soft material, respectively), and the principal direction of the stress tensor is parallel to the z-axis. That is, at this point the plane of maximum shear stress and the direction of the maximum shear rate are inclined to the layers at an angle of $\pi/4$. Along the arch connecting two extreme points A and C for each component the angle between the direction of maximum shear rate and the layer plane varies from 0 to $\pi/4$. Note that, as follows from Fig. 7, this angle is larger for the hard layer than for the soft one. This conclusion is consistent with the patterns of localized deformation zones described in Ref. [67], where shear zones in the hard layer were clearly distinguishable at an angle not exceeding $\pi/4$. These results are of a qualitative nature. The only model input they are based on is the assumed difference between the flow stresses of the two kinds of constituent layers.

Let us now outline possible variants of the behavior of a hard layer fragment in the soft matrix. It is determined by several factors, including the mechanical properties of the material and its environment, the strain accumulated in the latter, the geometry of the fragment, the character of its interaction with the environment, etc. Depending on the conditions, the fragment either deforms under the action of the environment or flows in it, without being deformed. In the former case, further fragmentation in smaller pieces is possible; their evolution will, in turn, be governed by the factors mentioned above. Iterated continually, this process will result in a gradual occupation of the sample volume with progressively smaller particles of the hard material.

A consequence of this particle dispersion process will be a strengthening of the soft matrix, which affects the further evolution of the sample structure. Obviously, here we are dealing with a self-organizing system [76] whose behavior can follow different scenarios depending on the fraction of the hard material, its distribution in the volume of the initial sample, and the HPT conditions.

To correlate the results of the structural studies (see Section 3.2) and computer simulations (Section 3.5), we consider this problem in a general form. We posit that in the case of complete adhesion of the fragment to the matrix at the interface, the behavior of the fragment is primarily determined by the dimensionless quantities $\xi = d/H$, and $\varsigma = \sigma_m/\sigma_f$ introduced above. We further hypothesize that there is a functional dependence between the two of the form $\xi = F(\varsigma)$ and that there exist a critical value ξ_c of ξ such that for $\xi < \xi_c$ the fragment does not experience plastic deformation. From general considerations, the validity of this hypothesis is plausible, as an excessively soft environment of a fragment and its very large distance from the anvils reduce the possibility of a transition of the fragment deformation into the plastic regime. Accordingly, $F(\varsigma)$ is a decreasing function. In the absence of a surrounding material ($\varsigma = 0$) a fragment can be deformed only by the plates, so that $F(0) = 1$. In the other limit case when the material is homogeneous ($\varsigma = 1$) it deforms throughout the entire bulk, so that $F(1) = 0$. It is obvious from the data obtained in the numerical experiment that they completely confirm the veracity of the proposed hypothesis.

We applied the above hypothesis and represented the evolution of the system on the (ξ, ς) plane. Each fragment is mapped on this plane as a

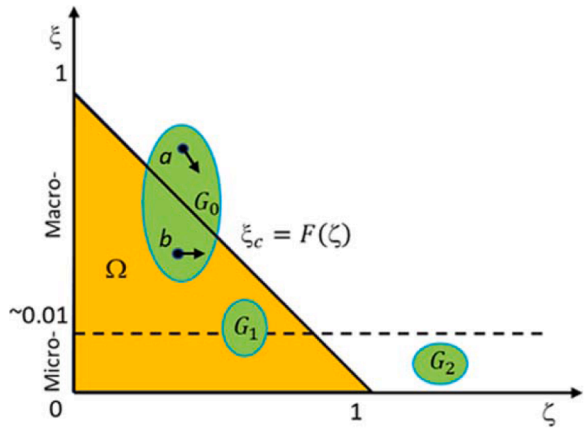

Fig. 8. Graphical representation of the evolution of a hard fragment in a soft matrix. Fragments of hard matter evolve from G_0 to G_2 under the action of HPT. Ω denotes the region where hard fragments do not undergo deformation. See the text for a detailed description.

representative point. However, the converse is not true, as multiple fragments with their environment may be represented by the same point on the plane. Since the fragments are randomly distributed in size, but as a rule have different environments, the entire solid body is represented by a certain region G on the (ξ, ς) plane. This region evolves during the HPT process. For a qualitative analysis, we assume that the function $F(\varsigma)$ is linear. In this case, the condition $\xi < F(\varsigma)$ generates a right triangle on the (ξ, ς) plane. This area is denoted as Ω in Fig. 8.

The pertinent geometrical representation of a fragment evolution during HPT is shown in Fig. 8. The region G_0 corresponds to the initial stage of the fragmentation of the hard layer, when large pieces are formed in the bulk of the sample. These are represented by points such as *a* situated above the straight line $\xi = F(\varsigma)$. A small number of fragments of the hard material with much smaller dimensions also emerge concurrently. Such hard inclusions, represented by the points located below the straight line, do not strengthen the matrix (point *b*). As an illustration, Fig. 3a shows a typical structure of the near-axis area of a Cu-Mo-Cu laminate after 32 anvil revolutions. The shear strain in this zone of the sample is small, and the image corresponds to the initial stage of the Mo layer fragmentation.

Over the following stages of fragmentation, large pieces of the hard material experience plastic deformation and are further crushed into smaller parts. The smallest of them are gradually spread over the matrix and strengthen the surrounding soft phase (Fig. 3b). The concomitant changes of the system position on the (ξ, ς) plane are indicated by a slanted arrow at point *a*. Small inclusions remain undeformed, whilst the surrounding matrix hardens, as indicated by a horizontal arrow at point *b*. In the end, this leads to shrinkage of region G along the ξ-axis and its displacement to the right along the ς-axis.

Two outcomes of the system evolution are possible depending on the governing factors mentioned above, including the content of the solid material, its distribution in the volume, mechanical properties of the constituents, etc.:

(1) Region G is entirely inside Ω, shown as G_1 in Fig. 8, when the deformation and fragmentation of the solid inclusion stop completely, and it simply floats in the deforming soft matrix.
(2) Due to the dispersion hardening, the flow stress of the matrix exceeds that of the hard material and region G leaves Ω. Then the deformation and fragmentation of the hard material continue (see region G_2 in Fig. 8).

As already mentioned, it can be assumed that this occurs in a self-similar manner (see the discussion below). As a result, a fractal structure may develop. According to Ref. [77], a thick yield surface and a cloud of internal stresses correspond to this kind of structure – geometric objects related to G and reflecting the stochastic nature of the material in the space of the stress tensor.

Having done this analysis of the evolution of the laminate structure, we now turn to a discussion of the mechanism of laminate fragmentation during HPT. The results of the experiments discussed in Section 3.2. suggest that it can differ cardinally from the mechanism of ductile fracture of metallic materials during metalworking, such as forging, stamping, rolling, etc. It is commonly accepted that conventional metalworking involves the formation and coalescence of micro-pores in polycrystals, see e.g., the review [78]. With an increase in hydrostatic pressure, the efficiency of pore generation decreases, which explains the well-known effect of plasticity enhancement under pressure, discovered by P. Bridgman [79]. Most likely, the high pressure used in HPT processing, which is a multiple of pressure levels used in metal forming operations, almost completely suppresses the micro-porosity formation. The random velocity field characteristic of the 'solid state turbulence' breaks the fragments of the harder material along high-angle grain boundaries formed as a result of large plastic strain [67].

Fig. 3 supports the viability of such a mechanism. It shows a typical Cu-Mo-Cu laminate structure at the late stages of the Mo layer fragmentation. Statistical analysis of the structure shown in Fig. 3a, without taking into account large particle outliers, leads to a lognormal size distribution of small fragments (Fig. S3d), known for self-similar crushing or milling [80]. These fragments are randomly oriented single crystals of molybdenum, which is confirmed by the misorientation distribution being similar to the Mackenzie distribution for non-textured polycrystals (Fig. S3d) [81]. This type of statistics is a characteristic feature of submicron-scale structures formed in metallic materials under large plastic strains [80]. This is consistent with the hypothesis that such small fragments were first formed in the bulk of a larger particle, which was subsequently crushed along high-angle grain boundaries. Fig. 3c offers an illustration for this. It displays a vortex that tears off fragments from a large particle, visible at the left-hand side of the picture. The process described above is iterative. It works in the same way until some critically small size of fragment is reached below which no further comminution takes place According to [82], this self-similar repeatability is an attribute of a self-organizing process.

5. Conclusions

We conducted an in-depth study on the behavior of a three-layer sandwich structure, representative of a broader class of laminated structures, at large strains A pair of constituent elemental layers (copper and molybdenum) with a significant contrast in hardness and yield strength was deliberately chosen for the following reasons. First, to demonstrate that the experimentally observed fragmentation of the harder constituent under severe plastic deformation by HPT is a natural consequence of this contrast in mechanical properties. Second, the copper-molybdenum pair serves as a classic example of an immiscible system that allows the analysis of mechanical mixing under enormously high shear deformation.

The main results of this study can be summarized as follows: The stress state of the hard phase is more heterogeneous than that of the soft one, and the presence of an axial component of the upsetting deformation leads to repeated strain localization in the molybdenum layer and its subsequent fragmentation into individual particles. Depending on the size and shape of a particle thus produced and its stress-strain state, it can either move and rotate as a whole without deformation or undergo further elongation and fragmentation. In this scenario, the softer copper phase is strengthened due to strain hardening, grain refinement, and dispersion strengthening. This strengthening of the soft phase, in turn, leads to further fragmentation of the hard phase. As a result, interesting self-similarity effects are observed. This is confirmed by the lognormal distribution of molybdenum particle sizes as well as by the results of nanoindentation tests. Mutual solubility on the order of a few atomic

percent reliably detected by atom probe tomography and energy dispersive X-ray analysis surpasses the equilibrium limits by far. This finding suggests the occurrence of mixing at the atomic scale.

In summary, the integrative approach combining several experimental techniques with numerical simulations employed in this study elucidated a complex interplay between microstructural changes in deforming Cu-Mo-Cu laminates and the associated mechanical properties. It provided valuable insights in the mechanisms underlying the material behavior under HPT conditions.

Data statement

The raw data for the results demonstrated in this study are available in KIT repository at https://doi.org/10.35097/1825.

Declaration of competing interests

The authors declare that they have no known competing financial interests or personal relationships that could have appeared to influence the work reported in this paper.

Acknowledgements

This research was performed as part of the Helmholtz Joint Laboratory Model Driven Materials Characterization (MDMC). The authors gratefully acknowledge funding of this study received from the Volkswagen Foundation through the Cooperation Project Az.: 97 751. Partial support from the Karlsruhe Nano Micro Facility (KNMFi, https://www.knmf.kit.edu), a Helmholtz Research Infrastructure at Karlsruhe Institute of Technology (KIT, www.kit.edu, proposal #2022-029-031547) is also acknowledged. The purchase of KLA nanoindenter iNano was enabled by 3DMM2O - Cluster of Excellence (EXC-2082/1 – 390761711).

Supplementary materials

Supplementary material associated with this article can be found, in the online version, at doi:10.1016/j.actamat.2024.119804.

References

[1] B.B. Straumal, A.R. Kilmametov, Y. Ivanisenko, L. Kurmanaeva, B. Baretzky, Y. O. Kucheev, P. Zięba, A. Korneva, D.A. Molodov, Phase transitions during high pressure torsion of CuCo alloys, Mater. Lett. 118 (2014) 111–114, https://doi.org/10.1016/j.matlet.2013.12.042.

[2] Y. Huang, S. Sabbaghianrad, A.I. Almazrouee, K.J. Al-Fadhalah, S.N. Alhajeri, T. G. Langdon, The significance of self-annealing at room temperature in high purity copper processed by high-pressure torsion, Mater. Sci. Eng. A. 656 (2016) 55–66, https://doi.org/10.1016/j.msea.2016.01.027.

[3] N. Lugo, N. Llorca, J.M.M. Cabrera, Z. Horita, Microstructures and mechanical properties of pure copper deformed severely by equal-channel angular pressing and high pressure torsion, Mater. Sci. Eng. A. 477 (2008) 366–371, https://doi.org/10.1016/j.msea.2007.05.083.

[4] J. Čížek, M. Janeček, O. Srba, R. Kužel, Z. Barnovská, I. Procházka, S. Dobatkin, Evolution of defects in copper deformed by high-pressure torsion, Acta Mater 59 (2011) 2322–2329, https://doi.org/10.1016/j.actamat.2010.12.028.

[5] X.Z. Liao, Y.H. Zhao, Y.T. Zhu, R.Z. Valiev, D.V. Gunderov, Grain-size effect on the deformation mechanisms of nanostructured copper processed by high-pressure torsion, J. Appl. Phys. 96 (2004) 636–640, https://doi.org/10.1063/1.1757035.

[6] B.B. Straumal, S.G. Protasova, A.A. Mazilkin, B. Baretzky, D. Goll, D.V. Gunderov, R.Z. Valiev, Effect of severe plastic deformation on the coercivity of Co–Cu alloys, Philos. Mag. Lett. 89 (2009) 649–654, https://doi.org/10.1080/09500830903246268.

[7] C. Tang, H. Li, S. Li, Effect of processing route on grain refinement in pure copper processed by equal channel angular extrusion, Trans. Nonferrous Met. Soc. China. 26 (2016) 1736–1744, https://doi.org/10.1016/S1003-6326(16)64286-3.

[8] Y. Beygelzimer, R. Kulagin, Y. Estrin, L.S. Toth, H.S. Kim, M.I. Latypov, Twist extrusion as a potent tool for obtaining advanced engineering materials: a review, Adv. Eng. Mater. 19 (2017) 1600873, https://doi.org/10.1002/ADEM.201600873.

[9] Y. Beygelzimer, D. Prilepo, R. Kulagin, V. Grishaev, O. Abramova, V. Varyukhin, M. Kulakov, Planar Twist Extrusion versus Twist Extrusion, J. Mater. Process. Technol. 211 (2011) 522–529, https://doi.org/10.1016/J.JMATPROTEC.2010.11.006.

[10] M. Shamsborhan, M. Ebrahimi, Production of nanostructure copper by planar twist channel angular extrusion process, J. Alloys Compd. 682 (2016) 552–556, https://doi.org/10.1016/j.jallcom.2016.05.012.

[11] Z.N. Mao, R.C. Gu, F. Liu, Y. Liu, X.Z. Liao, J.T. Wang, Effect of equal channel angular pressing on the thermal-annealing-induced microstructure and texture evolution of cold-rolled copper, Mater. Sci. Eng. A. 674 (2016) 186–192, https://doi.org/10.1016/j.msea.2016.07.050.

[12] P.C. Yadav, A. Sinhal, S. Sahu, A. Roy, S. Shekhar, Microstructural inhomogeneity in constrained groove pressed Cu-Zn alloy sheet, J. Mater. Eng. Perform. 25 (2016) 2604–2614, https://doi.org/10.1007/s11665-016-2142-0.

[13] K. Bryła, J. Morgiel, M. Faryna, K. Edalati, Z. Horita, Effect of high-pressure torsion on grain refinement, strength enhancement and uniform ductility of EZ magnesium alloy, Mater. Lett. 212 (2018) 323–326, https://doi.org/10.1016/j.matlet.2017.10.113.

[14] N. Sadasivan, M. Balasubramanian, R. Venkatesh, S. Vigneshram, T. Sunil, Influence of equal channel angular pressing in an acute angle die with a back pressure notch on grain refinement, torsion and mechanical properties of aluminium, Materwiss. Werksttech. 50 (2019) 155–164, https://doi.org/10.1002/mawe.201700102.

[15] R. Kulagin, Y. Beygelzimer, Y. Ivanisenko, A. Mazilkin, B. Straumal, H. Hahn, Instabilities of interfaces between dissimilar metals induced by high pressure torsion, Mater. Lett. 222 (2018) 172–175, https://doi.org/10.1016/j.matlet.2018.03.200.

[16] R.Z. Valiev, R.K. Islamgaliev, I.V. Alexandrov, Bulk nanostructured materials from severe plastic deformation, Prog. Mater. Sci. 45 (2000) 103–189, https://doi.org/10.1016/S0079-6425(99)00007-9.

[17] K. Bryła, M. Krystian, J. Horky, B. Mingler, K. Mroczka, P. Kurtyka, L. Lityńska-Dobrzyńska, Improvement of strength and ductility of an EZ magnesium alloy by applying two different ECAP concepts to processable initial states, Mater. Sci. Eng. A. 737 (2018) 318–327, https://doi.org/10.1016/j.msea.2018.09.070.

[18] E.A. Lukyanova, N.S. Martynenko, V.N. Serebryany, A.N. Belyakov, L.L. Rokhlin, S. V. Dobatkin, Y.Z. Estrin, Structure and mechanical and corrosion properties of a magnesium Mg–Y–Nd–Zr alloy after high pressure torsion, Russ. Metall. 2017 (2017) 912–921, https://doi.org/10.1134/S0036029517110088.

[19] S. Sabbaghianrad, S.A. Torbati-Sarraf, T.G. Langdon, An investigation of the limits of grain refinement after processing by a combination of severe plastic deformation techniques: a comparison of Al and Mg alloys, Mater. Sci. Eng. A. 712 (2018) 373–379, https://doi.org/10.1016/j.msea.2017.11.090.

[20] K. Tirsatine, H. Azzeddine, Y. Huang, T. Baudin, A.-L. Helbert, F. Brisset, D. Bradai, T.G. Langdon, An EBSD analysis of Fe-36 %Ni alloy processed by HPT at ambient and a warm temperature, J. Alloys Compd. 753 (2018) 46–53, https://doi.org/10.1016/j.jallcom.2018.04.194.

[21] M.Y. Alawadhi, S. Sabbaghianrad, Y. Huang, T.G. Langdon, Direct influence of recovery behaviour on mechanical properties in oxygen-free copper processed using different SPD techniques: HPT and ECAP, J. Mater. Res. Technol. 6 (2017) 369–377, https://doi.org/10.1016/j.jmrt.2017.05.005.

[22] B.B. Straumal, R. Kulagin, L. Klinger, E. Rabkin, P.B. Straumal, O.A. Kogtenkova, B. Baretzky, Structure Refinement and Fragmentation of Precipitates under Severe Plastic Deformation: a Review, Materials (Basel) 15 (2022) 601, https://doi.org/10.3390/ma15020601.

[23] J.M. Rosalie, P. Ghosh, J. Guo, O. Renk, Z. Zhang, Microstructural and texture evolution of copper-(chromium, molybdenum, tungsten) composites deformed by high-pressure-torsion, Int. J. Refract. Met. Hard Mater. 75 (2018) 137–146, https://doi.org/10.1016/J.IJRMHM.2018.04.008.

[24] S. Lee, Z. Horita, High-pressure torsion for pure chromium and niobium, Mater. Trans. 53 (2012) 38–45, https://doi.org/10.2320/matertrans.MD201131.

[25] K. Edalati, D. Akama, A. Nishio, S. Lee, Y. Yonenaga, J.M. Cubero-Sesin, Z. Horita, Influence of dislocation-solute atom interactions and stacking fault energy on grain size of single-phase alloys after severe plastic deformation using high-pressure torsion, Acta Mater. 69 (2014) 68–77, https://doi.org/10.1016/j.actamat.2014.01.036.

[26] R. Tejedor, K. Edalati, J.A. Benito, Z. Horita, J.M. Cabrera, High-pressure torsion of iron with various purity levels and validation of Hall-Petch strengthening mechanism, Mater. Sci. Eng. A. 743 (2019) 597–605, https://doi.org/10.1016/j.msea.2018.11.127.

[27] I.F. Mohamed, T. Masuda, S. Lee, K. Edalati, Z. Horita, S. Hirosawa, K. Matsuda, D. Terada, M.Z. Omar, Strengthening of A2024 alloy by high-pressure torsion and subsequent aging, Mater. Sci. Eng. A. 704 (2017) 112–118, https://doi.org/10.1016/j.msea.2017.07.083.

[28] K. Edalati, H. Shao, H. Emami, H. Iwaoka, E. Akiba, Z. Horita, Activation of titanium-vanadium alloy for hydrogen storage by introduction of nanograins and edge dislocations using high-pressure torsion, Int. J. Hydrogen Energy. 41 (2016) 8917–8924, https://doi.org/10.1016/j.ijhydene.2016.03.146.

[29] M. Isik, M. Niinomi, K. Cho, M. Nakai, H. Liu, H. Yilmazer, Z. Horita, S. Sato, T. Narushima, Microstructural evolution and mechanical properties of biomedical Co–Cr–Mo alloy subjected to high-pressure torsion, J. Mech. Behav. Biomed. Mater. 59 (2016) 226–235, https://doi.org/10.1016/j.jmbbm.2015.11.015.

[30] M. Isik, M. Niinomi, H. Liu, K. Cho, M. Nakai, Z. Horita, S. Sato, T. Narushima, H. Yilmazer, M. Nagasako, Grain refinement mechanism and evolution of dislocation structure of Co–Cr–Mo alloy subjected to high-pressure torsion, Mater. Trans. 57 (2016) 1109–1118, https://doi.org/10.2320/matertrans.M2016052.

[31] T. Hongo, K. Edalati, H. Iwaoka, M. Arita, J. Matsuda, E. Akiba, Z. Horita, High-pressure torsion of palladium: hydrogen-induced softening and plasticity in ultrafine grains and hydrogen-induced hardening and embrittlement in coarse grains, Mater. Sci. Eng. A. 618 (2014) 1–8, https://doi.org/10.1016/j.msea.2014.08.074.

[32] K. Edalati, K. Imamura, T. Kiss, Z. Horita, Equal-channel angular pressing and high-pressure torsion of pure copper: evolution of electrical conductivity and hardness with strain, Mater. Trans. 53 (2012) 123–127, https://doi.org/10.2320/matertrans.MD201109.
[33] A. Hanna, H. Azzeddine, R. Lachhab, T. Baudin, A.-L.L. Helbert, F. Brisset, Y. Huang, D. Bradai, T.G. Langdon, Evaluating the textural and mechanical properties of an Mg-Dy alloy processed by high-pressure torsion, J. Alloys Compd. 778 (2019) 61–71, https://doi.org/10.1016/j.jallcom.2018.11.109.
[34] Y.I. Bourezg, H. Azzeddine, T. Baudin, A.-L. Helbert, Y. Huang, D. Bradai, T. G. Langdon, Texture and microhardness of Mg-Rare Earth (Nd and Ce) alloys processed by high-pressure torsion, Mater. Sci. Eng. A. 724 (2018) 477–485, https://doi.org/10.1016/j.msea.2018.03.114.
[35] P. Bazarnik, Y. Huang, M. Lewandowska, T.G. Langdon, Enhanced grain refinement and microhardness by hybrid processing using hydrostatic extrusion and high-pressure torsion, Mater. Sci. Eng. A. 712 (2018) 513–520, https://doi.org/10.1016/j.msea.2017.12.007.
[36] S.A. Torbati-Sarraf, S. Sabbaghianrad, R.B. Figueiredo, T.G. Langdon, Orientation imaging microscopy and microhardness in a ZK60 magnesium alloy processed by high-pressure torsion, J. Alloys Compd. 712 (2017) 185–193, https://doi.org/10.1016/j.jallcom.2017.04.054.
[37] D.M. Marulanda Cardona, J. Wongsa-Ngam, H. Jimenez, T.G. Langdon, Effects on hardness and microstructure of AISI 1020 low-carbon steel processed by high-pressure torsion, J. Mater. Res. Technol. 6 (2017) 355–360, https://doi.org/10.1016/j.jmrt.2017.05.002.
[38] A. Korneva, B. Straumal, A. Kilmametov, L. Lityńska-Dobrzyńska, G. Cios, P. Bała, P. Zięba, Effect of high pressure torsion on microstructure of Cu-Sn alloys with different content of Hume Rothery phase, Mater. Charact. 118 (2016) 411–416, https://doi.org/10.1016/j.matchar.2016.06.019.
[39] B.B. Straumal, V. Pontikis, A.R. Kilmametov, A.A. Mazilkin, S.V. Dobatkin, B. Baretzky, Competition between precipitation and dissolution in Cu–Ag alloys under high pressure torsion, Acta Mater 122 (2017) 60–71, https://doi.org/10.1016/j.actamat.2016.09.024.
[40] B.B. Straumal, A.R. Kilmametov, O.A. Kogtenkova, A.A. Mazilkin, B. Baretzky, A. Korneva, P. Zieba, P. Zięba, Phase transitions in copper–silver alloys under high pressure torsion, Int. J. Mater. Res. 110 (2019) 608–613, https://doi.org/10.3139/146.111784.
[41] B.B. Straumal, A.R. Kilmametov, B. Baretzky, O.A. Kogtenkova, P.B. Straumal, L. Lityńska-Dobrzyńska, R. Chulist, A. Korneva, P. Zięba, High pressure torsion of Cu–Ag and Cu–Sn alloys: limits for solubility and dissolution, Acta Mater. 195 (2020) 184–198, https://doi.org/10.1016/j.actamat.2020.05.055.
[42] I. Sabirov, R. Pippan, Formation of a W-25% Cu nanocomposite during high pressure torsion, Scr. Mater. 52 (2005) 1293–1298, https://doi.org/10.1016/j.scriptamat.2005.02.017.
[43] D. Edwards, I. Sabirov, W. Sigle, R. Pippan, Microstructure and thermostability of a W–Cu nanocomposite produced via high-pressure torsion, Philos. Mag. 92 (2012) 4151–4166, https://doi.org/10.1080/14786435.2012.704426.
[44] I. Sabirov, R. Pippan, Characterization of tungsten fragmentation in a W–25%Cu composite after high-pressure torsion, Mater. Charact. 58 (2007) 848–853, https://doi.org/10.1016/j.matchar.2006.08.001.
[45] A. Bachmaier, J. Schmauch, H. Aboulfadl, A. Verch, C. Motz, On the process of co-deformation and phase dissolution in a hard-soft immiscible Cu Co alloy system during high-pressure torsion deformation, Acta Mater. 115 (2016) 333–346, https://doi.org/10.1016/j.actamat.2016.06.010.
[46] A. Bachmaier, H. Aboulfadl, M. Pfaff, F. Mücklich, C. Motz, Structural evolution and strain induced mixing in Cu–Co composites studied by transmission electron microscopy and atom probe tomography, Mater. Charact. 100 (2015) 178–191, https://doi.org/10.1016/j.matchar.2014.12.022.
[47] A. Bachmaier, G.B. Rathmayr, M. Bartosik, D. Apel, Z. Zhang, R. Pippan, New insights on the formation of supersaturated solid solutions in the Cu–Cr system deformed by high-pressure torsion, Acta Mater. 69 (2014) 301–313, https://doi.org/10.1016/j.actamat.2014.02.003.
[48] K.T. Schwarz, J.M. Rosalie, S. Wurster, R. Pippan, A. Hohenwarter, Microstructure and failure characteristics of nanostructured molybdenum–copper composites, Adv. Eng. Mater. 22 (2020) 1900474, https://doi.org/10.1002/ADEM.201900474.
[49] J.M. Rosalie, J. Guo, R. Pippan, Z. Zhang, On nanostructured molybdenum–copper composites produced by high-pressure torsion, J. Mater. Sci. 52 (2017) 9872–9883, https://doi.org/10.1007/S10853-017-1142-2/FIGURES/10.
[50] M. Hosseini, N. Pardis, H. Danesh Manesh, M. Abbasi, D.-I. Kim, Structural characteristics of Cu/Ti bimetal composite produced by accumulative roll-bonding (ARB), Mater. Des 113 (2017) 128–136, https://doi.org/10.1016/j.matdes.2016.09.094.
[51] Y. Ivanisenko, W. Lojkowski, R.Z. Valiev, H.-J. Fecht, The mechanism of formation of nanostructure and dissolution of cementite in a pearlitic steel during high pressure torsion, Acta Mater. 51 (2003) 5555–5570, https://doi.org/10.1016/S1359-6454(03)00419-1.
[52] Y. Ivanisenko, R.K. Wunderlich, R.Z. Valiev, H.-J. Fecht, Annealing behaviour of nanostructured carbon steel produced by severe plastic deformation, Scr. Mater. 49 (2003) 947–952, https://doi.org/10.1016/S1359-6462(03)00478-0.
[53] J. Zrnik, R. Pippan, S. Scheriau, L. Kraus, M. Fujda, Microstructure and mechanical properties of UFG medium carbon steel processed by HPT at increased temperature, J. Mater. Sci. 45 (2010) 4822–4826, https://doi.org/10.1007/s10853-010-4482-8.
[54] S. Bayramoglu, C.H. Gür, I.V. Alexandrov, M.M. Abramova, Characterization of ultra-fine grained steel samples produced by high pressure torsion via magnetic Barkhausen noise analysis, Mater. Sci. Eng. A. 527 (2010) 927–933, https://doi.org/10.1016/j.msea.2009.09.006.
[55] J. Ning, E. Courtois-Manara, L. Kurmanaeva, A.V. Ganeev, R.Z. Valiev, C. Kübel, Y. Ivanisenko, Tensile properties and work hardening behaviors of ultrafine grained carbon steel and pure iron processed by warm high pressure torsion, Mater. Sci. Eng. A. 581 (2013) 8–15, https://doi.org/10.1016/j.msea.2013.05.008.
[56] Y. Todaka, Y. Miki, M. Umemoto, C.H. Wang, K. Tsuchiya, Tensile property of submicrocrystalline pure Fe produced by HPT-straining, Mater. Sci. Forum. 584–586 (2008) 597–602, https://doi.org/10.4028/www.scientific.net/MSF.584-586.597.
[57] D.H. Shin, K.-T. Park, Y.-S. Kim, Formation of fine cementite precipitates in an ultra-fine grained low carbon steel, Scr. Mater. 48 (2003) 469–473, https://doi.org/10.1016/S1359-6462(02)00512-2.
[58] F. Wetscher, A. Vorhauer, R. Stock, R. Pippan, Structural refinement of low alloyed steels during severe plastic deformation, Mater. Sci. Eng. A. 387–389 (2004) 809–816, https://doi.org/10.1016/j.msea.2004.01.096.
[59] Y. Ivanisenko, X. Sauvage, A. Mazilkin, A. Kilmametov, J.A. Beach, B.B. Straumal, Bulk nanocrystalline ferrite stabilized through grain boundary carbon segregation, Adv. Eng. Mater. 20 (2018) 1800443, https://doi.org/10.1002/adem.201800443.
[60] J.M. Cubero-Sesin, Z. Horita, Strengthening via microstructure refinement in bulk Al-4 mass% Fe alloy using high-pressure torsion, Mater. Trans. 53 (2012) 46–55, https://doi.org/10.2320/matertrans.MD201127.
[61] T. Aboud, B.-Z. Weiss, R. Chaim, Mechanical alloying of the immiscible system W-Cu, Nanostruct. Mater. 6 (1995) 405–408, https://doi.org/10.1016/0965-9773(95)00082-8.
[62] C. Aguilar, F. Castro, V. Martínez, D. Guzmán, F. de las Cuevas, L. Lozada, N. Vielma, Structural study of nanocrystalline solid solution of Cu–Mo obtained by mechanical alloying, Mater. Sci. Eng. A. 548 (2012) 189–194, https://doi.org/10.1016/j.msea.2012.03.105.
[63] C.H. Lee, S.H. Lee, Nanocrystalline formation in immiscible Cu-Mo system subjected to mechanical alloying, J. Nanosci. Nanotechnol. 7 (2007) 4057–4060, https://doi.org/10.1166/JNN.2007.069.
[64] N. Verma, N. Pant, J.A. Beach, J. Ivanisenko, Y. Ashkenazy, S. Dillon, P. Bellon, R. S. Averback, Effects of ternary alloy additions on the microstructure of highly immiscible Cu alloys subjected to severe plastic deformation: an evaluation of the effective temperature model, Acta Mater. 170 (2019) 218–230, https://doi.org/10.1016/J.ACTAMAT.2019.03.023.
[65] M. Pouryazdan, B.J.P. Kaus, A. Rack, A. Ershov, H. Hahn, Mixing instabilities during shearing of metals, Nat. Commun. 8 (2017) 1–7, https://doi.org/10.1038/s41467-017-01879-5.
[66] A. Gola, R. Schwaiger, P. Gumbsch, L. Pastewka, Pattern formation during deformation of metallic nanolaminates, Phys. Rev. Mater. 4 (2020) 013603, https://doi.org/10.1103/PhysRevMaterials.4.013603.
[67] V. Tavakkoli, A. Mazilkin, T. Scherer, M. Mail, Y. Beygelzimer, B. Baretzky, Y. Estrin, R. Kulagin, Instability of a molybdenum layer under deformation of a CuMoCu laminate by high-pressure torsion, Mater. Lett. 302 (2021) 130378, https://doi.org/10.1016/J.MATLET.2021.130378.
[68] N.K. Sundaram, A. Mahato, Y. Guo, K. Viswanathan, S. Chandrasekar, Folding in metal polycrystals: microstructural origins and mechanics, Acta Mater. 140 (2017) 67–78, https://doi.org/10.1016/J.ACTAMAT.2017.08.018.
[69] R.P. Chhabra, Non-Newtonian Fluids: an Introduction. Rheol. Complex Fluids, Springer, New York, New York, NY, 2010, pp. 3–34, https://doi.org/10.1007/978-1-4419-6494-6_1.
[70] QForm, (n.d.) https://www.qform3d.com/.
[71] G.J. Kleiser, B. Revil-Baudard, O. Cazacu, C.L. Pasiliao, Plastic deformation of polycrystalline molybdenum: experimental data and macroscopic model accounting for its anisotropy and tension–compression asymmetry, Int. J. Solids Struct. 75–76 (2015) 287–298, https://doi.org/10.1016/j.ijsolstr.2015.08.021.
[72] P.R. Subramanian, D.E. Laughlin, The Cu-Mo (Copper-Molybdenum) system, Bull. Alloy Phase Diagrams 11 (1990) 169–172, https://doi.org/10.1007/BF02841703.
[73] K.K. Chawla, Composite materials: science and engineering, third edition, Compos. Mater. Sci. Eng. Third Ed. (2012) 1–542, https://doi.org/10.1007/978-0-387-74365-3/COVER.
[74] Y. Beygelzimer, Y. Estrin, O. Davydenko, R. Kulagin, Gripping prospective of non-shear flows under high-pressure torsion, Materials (Basel) 16 (2023) 823, https://doi.org/10.3390/ma16020823.
[75] L.M. Kachanov, Fundamentals of the Theory of Plasticity, Dover Publications, Mineola, N.Y., 2004.
[76] H. Haken (Ed.), Synergetics, Springer Berlin Heidelberg, Berlin, Heidelberg, 1978, https://doi.org/10.1007/978-3-642-96469-5.
[77] Y.E. Beygelzimer, A.V. Spuskanyuk, The thick yield surface: idea and approach for investigating its structure, Philos. Mag. A. 79 (1999) 2437–2459, https://doi.org/10.1080/01418619908214293.
[78] T.S. Cao, Models for ductile damage and fracture prediction in cold bulk metal forming processes: a review, Int. J. Mater. Form. 10 (2017) 139–171, https://doi.org/10.1007/s12289-015-1262-7.
[79] P.W. Bridgman, Studies in Large Plastic Flow and Fracture, Harvard University Press, 1964, https://doi.org/10.4159/harvard.9780674731349.
[80] Y. Beygelzimer, Grain refinement versus voids accumulation during severe plastic deformations of polycrystals: mathematical simulation, Mech. Mater. 37 (2005) 753–767, https://doi.org/10.1016/j.mechmat.2004.07.006.
[81] J.K. Mackenzie, Second paper on statistics associated with the random disorientation of cubes, Biometrika 45 (1958) 229, https://doi.org/10.2307/2333059.
[82] A.N. Kolmogorov, On the lognormal distribution law for particle sizes on crushing, Dokl. Akad. Nauk (1941) 2.

[83] M.A. Meyers, K.K. Chawla, M.A. Meyers, K. Kumar, C. Frontmatter, Mechanical behavior of materials-mechanical behavior of materials more information, (n.d.). www.cambridge.org (accessed November 15, 2023).
[84] K.-M. Xue, Z. Wang, X. Wang, Y.-F. Zhou, P. Li, Nano-indentation nanohardness and elastic modulus evolution of molybdenum processed by high-pressure torsion, Mater. Sci. Technol. 37 (2021) 716–724, https://doi.org/10.1080/02670836.2020.1740863.
[85] S. Lee, K. Edalati, Z. Horita, Microstructures and mechanical properties of pure V and Mo processed by high-pressure torsion, Mater. Trans. 51 (2010) 1072–1079, https://doi.org/10.2320/matertrans.M2009375.
[86] X. Wang, P. Li, Y. Huang, N. Gao, T.G. Langdon, Microstructure and microhardness evolution in pure molybdenum processed by high-pressure torsion, Adv. Eng. Mater. 22 (2020), https://doi.org/10.1002/adem.201901022.
[87] X.H. An, S.D. Wu, Z.F. Zhang, R.B. Figueiredo, N. Gao, T.G. Langdon, Evolution of microstructural homogeneity in copper processed by high-pressure torsion, Scr. Mater. 63 (2010) 560–563, https://doi.org/10.1016/j.scriptamat.2010.05.030.
[88] A. Rijal, S.P. Singh, J.-K. Han, M. Kawasaki, P. Kumar, Effect of high-pressure torsion on hardness and electrical resistivity of commercially pure Cu, Adv. Eng. Mater. (2020) 22, https://doi.org/10.1002/adem.201900547.
[89] J. Xu, J. Li, C.T. Wang, D. Shan, B. Guo, T.G. Langdon, Evidence for an early softening behavior in pure copper processed by high-pressure torsion, J. Mater. Sci. 51 (2016) 1923–1930, https://doi.org/10.1007/s10853-015-9499-6.
[90] Z. Horita, T.G. Langdon, Microstructures and microhardness of an aluminum alloy and pure copper after processing by high-pressure torsion, Mater. Sci. Eng. A. 410–411 (2005) 422–425, https://doi.org/10.1016/j.msea.2005.08.133.